

Received January 5, 2022, accepted January 21, 2022, date of publication January 27, 2022, date of current version February 4, 2022.

Digital Object Identifier 10.1109/ACCESS.2022.3146866

# Lift Generation by a Miniature Piezoelectric Ultrasonic Motor-Driven Rotary-Wing for Pico Air Vehicles

ERIC TAN KAI CHIANG<sup>1</sup>, (Member, IEEE), TAKATERU URAKUBO<sup>2</sup>, (Member, IEEE), AND TOMOAKI MASHIMO<sup>1</sup>, (Member, IEEE)

<sup>1</sup>Department of Mechanical Engineering, Toyohashi University of Technology, Toyohashi, Aichi 441-8580, Japan

<sup>2</sup>Department of Information Science, Graduate School of System Informatics, Kobe University, Kobe 657-8501, Japan

Corresponding author: Tomoaki Mashimo (mashimo@me.tut.ac.jp)

This work was supported in part by the Japan Society for the Promotion of Science (JSPS) KAKENHI under Grant 19H02110.

**ABSTRACT** Actuators are key components for further miniaturization of insect-scale microrobots. It is challenging to create a new miniature actuator suited for rotary-wing pico aerial vehicles (PAVs), which have a wing span of a few centimeters and a mass of a few grams. In this paper, we propose a miniature piezoelectric ultrasonic motor that permits high-speed rotation at a sufficient torque to achieve the flight of the simplest device comprising the proposed motor and rotor blades. The prototype motor, which employs a bending vibration mode as a principle, measures  $1.6 \text{ mm} \times 1.6 \text{ mm} \times 2 \text{ mm}$  and weighs 25 mg. The experimental results show that the miniature motor rotates rotor blades having a length of 20 mm with an angular velocity of over 1800 rad/s. The thrust force generated from this system exceeds its total mass of 110 mg and successfully lifts the system. Although the flight is tethered, the set of the proposed motor and rotor blades demonstrates a takeoff that represents the possibility of rotary-wing PAVs.

**INDEX TERMS** Micro air vehicles, propellers, micromotors, microactuators, microfabrications.

## I. INTRODUCTION

Miniature unmanned aerial vehicles (UAVs) have a significant impact on society, based on their diverse applications ranging from the media and entertainments to deliveries and inspections [1]. The smallest class of miniature UAVs, having a wing span of a few centimeters and a mass of a few grams, are called pico air vehicles (PAVs) [2], [3]. (They are also called nano/pico drones or insect-scale flying robots.) The main purposes of PAVs are to perform various tasks in environments that people cannot access, such as narrow and confined spaces and high-risk environments. For instance, search and rescue might be one example to be applied; Survivors can be helped more quickly if PAVs can gather more accurate information at a disaster site.

Generally, reducing the size of UAVs increases their practicality to access targets in narrower spaces. However, the miniaturization into centimeter scales is challenging because of several problems [4]. One such problem is the optimization of flight mechanisms in a low Reynolds number

environment. Since it has been shown that flapping aerial vehicles mimicking the flight mechanism of insects and birds are superior, most studies aim to downsize hardware by biological inspiration [5]–[7]. These biomimetic flying microrobots typically apply three aerodynamic mechanisms, i.e., delayed stall, rotation circulation, and wake capture, to improve flapping flight [8]. One of using such mechanisms is Harvard's RoboBee known as the most successful insect-scale flapping-wing robot with a wing span of 30 mm [9], [10]. Employing biological motions is an effective way to reduce the size of flying microrobots, but designing a millimeter-scale mechanism that mimics the motion of insects or birds involves difficulties, such as the selection of actuators and a complex fabrication process.

The types of wings that are advantageous in a low Reynolds number environment are of great interest in the field of aerodynamics. Lentink *et al.* provided a deep insight on the lift force of a fixed-wing, flapping-wing, and rotary-wing at various Reynolds numbers [11]. They discovered that the flapping-wing and rotary-wing generate twice the lift and drag as compared to the fixed-wing, and the rotary-wing is the most efficient among the three wings. This result

The associate editor coordinating the review of this manuscript and approving it for publication was Halil Ersin Soken.

**TABLE 1.** Characteristics of the existing miniature ultrasonic motors at a few millimeter scale.

	Dimensions	Hole dia.	Weight	Vibration mode	Natural frequency	Torque	Angular velocity	Efficiency
	mm	mm	mg		kHz	$\mu\text{Nm}$	rad/s	%
[24][25]	1.6×1.6×1	0.7	22	3 waves	1032	9.9	881	0.79
[25]	1.6×1.6×2	0.7	37	Bending	575	9.9	2440	1.52
[26]	3.2×3.2×2	1.4	138	3 waves	510	60	500	6.7
Proposed	1.6×1.6×2	0.7	37	Bending	585	22.0	2200	2.9

indicates that miniaturizing rotary-wing PAVs is worthwhile. This insight has been partly demonstrated by a rotary-wing PAV named Piccollissimo using a propeller with a diameter of 28 mm, which is currently known as the world's smallest drone [12].

The miniaturization of rotary-wing PAVs is an attractive topic in the field of microrobotics, but a lack of tiny rotary actuators restricts further developments. This study aims to present a millimeter-scale piezoelectric ultrasonic motor that can satisfy the specifications of a rotary-wing PAV. The prototype stator in this study comprises a metal cuboid of 1 mm × 1 mm × 2 mm and four piezoelectric plates adhered to its sides. Rotor blades with a length of 20 mm are assembled to the prototype motor, and an experiment is conducted to show the feasibility of the miniature flight device. The main contribution of this paper is the 1–2 millimeter-scale rotary ultrasonic motor that enables the flight of a centimeter-scale aerial vehicle (rotary-wing PAV), as well as its first flight demonstration.

The remainder of this paper is organized as follows. We describe the selection of actuators, the principle of the miniature ultrasonic motor, and its dynamics with the rotor blades in Section II. Section III shows the construction of the prototype motor and evaluates the motor performance measures. In Section IV, the assembly of the motor with the rotor blades is tested in the experiment.

## II. PRINCIPLE AND DESIGN

### A. SELECTION OF ACTUATORS FOR ROTARY-WING PAVS

To achieve micromotors with sufficient power, many researchers have demonstrated their prototypes in the past 40 years [13], [14]. However, these micromotors have not been able to satisfy the specifications for smaller PAVs. Electromagnetic motors are widely used in flying robots because of their high-speed rotation, but have difficulties in the miniaturization of their components such as coils and bearings [15]. Moreover, they face severe torque dissipation due to the scaling of physical effects [16]–[18]. In other words, at a few millimeter scale, electromagnetic motors cannot remain a sufficient torque for lift generation. Electrostatic motors can be miniaturized to less than 1 mm by using micro-electro-mechanical system (MEMS) processes [19], [20], but their weak output force limits applications. Ultrasonic motors,

which use the piezoelectric effect as a principle, are considered the most practical micromotors usable at the millimeter scale because of their simple structure and high torque density [21], [22]. For example, a rotary type of Squiggle motor, which is a commercially available millimeter-scale actuator, can generate over 1000 rad/s with a large torque [23]. Because ultrasonic motors inherently deliver high-torque at low-speed, changes in the design are required to reach the desired speeds (approximately 2000 rad/s) for PAVs. Existing miniature ultrasonic motors have been compared in review papers (e. g., [14], [22]).

When designing a motor of just a few millimeters in size, a simple design is necessary to ensure the microfabrication and the assembly of the components. We have proposed miniature ultrasonic motors with the simple design comprising a cuboid and piezoelectric plates. Table 1 summarizes the characteristics of the existing miniature ultrasonic motors with the similar design at a few millimeter scale. A small motor can obtain a high angular velocity of more than 800 rad/s [24], [25]. A larger motor increases the torque up to 60  $\mu\text{Nm}$  but reduces the speed [26]. Recently, a relatively long stator with a side length of 1.6 mm a height of 2 mm can spin the rotor with a high speed of more than 2400 rad/s by using a bending mode as the principle [25]. This speed satisfies the desired value for PAVs, but the torque is still low. In this paper, we develop the bending mode-based micromotor with a sufficient torque that enables the flight.

### B. DRIVING PRINCIPLE AND DESIGN

We develop the bending mode-based motor as a promising actuator for PAVs. The principle of ultrasonic motors using the bending mode has been explained in detail [27], [28]. Fig. 1(a) shows the design of the stator. It comprises a rectangular cuboid with a side length of 1 mm and a height of 2 mm. There is a hole with a diameter of 0.7 mm at the center of the stator, and four piezoelectric plates (PZT1–PZT4) with a thickness of 0.3 mm and a width of 0.8 mm are attached to the four sides of the cuboid, respectively. Fig. 1(b) shows the first-order bending vibration mode of the rectangular cuboid stator. This mode shape can be estimated by a modal analysis using a finite element method (FEM) software. In addition to this bending mode, the stator generates another bending mode orthogonally. When the voltages excite the two bending

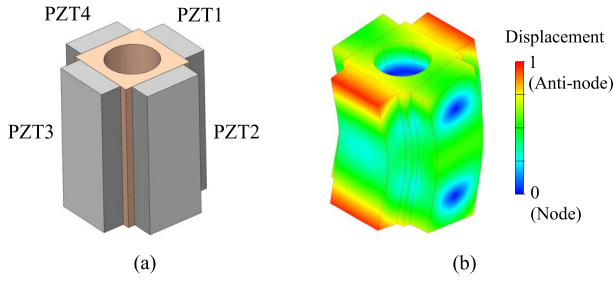


**FIGURE 1. (a) Design of the stator. (b) First-order bending vibration mode of the stator.**

modes with a temporal phase difference of  $\pi/2$ , the stator generates a “wobble motion”. During this period, the end of the stator generates an elliptical motion. This elliptical motion transfers energy to the rotor contacted to the stator’s end.

To excite the bending mode in the stator, voltage  $E_1 = A_E \sin(2\pi f_E t)$  and its reverse-phase voltage  $E_3 = -A_E \sin(2\pi f_E t)$  are applied to PZT1 and PZT3, respectively, where  $A_E$  and  $f_E$  are the amplitude and the frequency of the voltages, respectively. The frequency  $f_E$  is adjusted to be equal to the natural frequency of the bending mode. When these voltages are applied, PZT1 expands and PZT3 contracts or vice versa. Through repeated expansion and contraction, the bending mode is excited in the stator. Likewise, when voltage  $E_2 = A_E \cos(2\pi f_E t)$  and its reverse-phase voltage  $E_4 = -A_E \cos(2\pi f_E t)$  are applied to PZT2 and PZT4, respectively, the stator generates the same mode with an angular difference of  $\pi/2$ , forming an elliptical motion that rotates the rotor.

**C. RELATIONSHIP BETWEEN EQUATION OF ROTATIONAL MOTION AND ANTI-TORQUE**

We summarize the equations of motion for the miniature piezoelectric ultrasonic motor when it spins a load or rotor blades. Thrust and anti-torque are generated by the rotation of the rotor blades.

In ultrasonic motors that use a friction drive as their principle, the rotor and the stator are in contact with each other, and a contact point on the stator oscillates according to the frequency of the input voltages. The difference between the velocities of contact points on the rotor and the stator causes a frictional force that depends on the preload, and this force is transferred as a driving torque to the rotor. In general, the transient responses of ultrasonic motors are modeled as a first-order system, but an error occurs at a high angular velocity [29]. This is because the viscous friction in the model is slightly higher than the actual. From this perspective on the driving mechanism, when the rotor spins with an angular velocity of  $\omega$ , the equation of rotational motion for the motor can be represented as follows:

$$J\dot{\omega} = k(N) \tanh(a(\omega_c - \omega)) - \mu(N)\text{sign}(\omega) \quad (1)$$

where  $J$  is the moment of inertia of a rotor and a load. The driving torque is the first term in the right-hand side of (1)

where  $\omega_c$  is a specific angular velocity that is determined according to the input voltage with a specified frequency and  $k(N)$  is a coefficient that depends on the preload  $N$ . We use the function  $\tanh$ , supposing that the frictional force on the contact surface between the rotor and the stator is linearly proportional to  $\omega_c - \omega$ , if  $|\omega_c - \omega|$  is small, and is a constant, if  $|\omega_c - \omega|$  is large. In addition, we introduce a Coulomb friction as the second term in the right-hand side of (1), because the oscillation of the contact point on the stator is not uniform. The coefficient  $\mu(N)$  also depends on the preload  $N$ .

We next consider the equations of motion for the ultrasonic motor with rotor blades. Thrust  $T$  and anti-torque  $Q$  generated from the blades rotating with the angular velocity  $\omega$  are usually expressed as follows:

$$T = \rho\pi R^4 C_T \omega^2, \quad (2)$$

$$Q = \rho\pi R^5 C_Q \omega^2, \quad (3)$$

where  $C_T$  and  $C_Q$  are the thrust coefficient and the torque coefficient, respectively, and  $R$  is the length of each blade. Assuming that the chord of each blade is a constant  $c$  along the span and that the section drag coefficient  $C_d$  is also constant at each cross-section, the following equation can be derived for a rotor with two blades in hover from the momentum theory and the blade element theory [30], [31]:

$$C_Q = \frac{C_T^{\frac{3}{2}}}{\sqrt{2}} + \frac{c \cdot C_d}{4\pi R}. \quad (4)$$

By modifying (1) with the anti-torque in (3), we obtain the equation of rotational motion for the ultrasonic motor with rotor blades:

$$J_p \dot{\omega} = k(N) \tanh(a(\omega_c - \omega)) - \mu(N)\text{sign}(\omega) - \rho\pi R^5 C_Q \omega^2, \quad (5)$$

where  $J_p$  is the moment of inertia of the rotor and the blades. It is noted that the first and second terms in the right-hand side of (5) are the same as those in (1), despite the inertia of the rotor having changed and the addition of the anti-torque. On the other hand, when the motor with rotor blades is attached to a flight device, the thrust in (2) causes the translational motion of the device along with other forces. For the vertically upward thrust, the equation of motion for the flight device’s height  $h$  is written as follows:

$$M\ddot{h} = -Mg + \rho\pi R^4 C_T \omega^2 + F_e, \quad (6)$$

where  $M$  is the mass of the device including the blades,  $g$  is the gravitational acceleration, and  $F_e$  denotes other external forces in a vertical direction.

**III. EVALUATION OF THE MINIATURE PIEZOELECTRIC ULTRASONIC MOTOR**

**A. MOTOR PROTOTYPE**

Fig. 2(a) shows the stator of the miniature piezoelectric ultrasonic motor. The stator comprises a phosphor bronze cuboid and four piezoelectric plates (C-213, Fuji ceramics, Fujinomiya, Japan). The piezoelectric plates are polarized

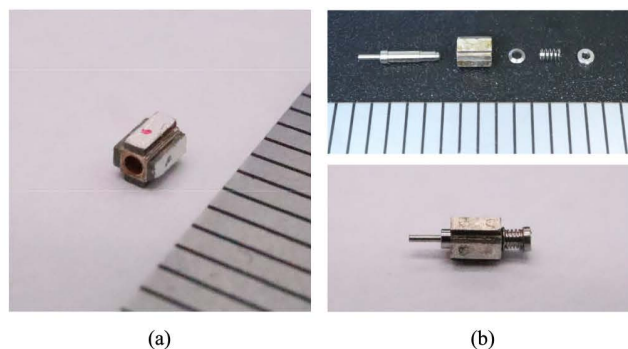


**FIGURE 2.** (a) Prototype stator. (b) Components for miniature ultrasonic motor (top) and the assembly (bottom).

between the two electrodes in the thickness direction. They have the same polarization orientation, which is positive at the external surfaces. All the components of the stator can be fabricated using conventional machining processes. The metallic cuboid is milled from a block, and the piezoelectric plates are cut using a dicing saw. Electrically conductive epoxy adhesive is used to bond the four piezoelectric plates to the metal cuboid. The prototype stator measures  $1.6 \text{ mm} \times 1.6 \text{ mm} \times 2 \text{ mm}$  and weighs 25 mg.

The top of Fig. 2(b) shows the components for the miniature ultrasonic motor: a rotor, stator, a tapper, micro-coil spring, and a stopper. It is known that in ultrasonic motors, an appropriate preload enhances the motor torque. When the preload mechanism is assembled, the microspring shrinks and generates a preload between the stator and rotor. To evaluate the motor performance, three microsprings with different spring coefficients are prepared; the springs are designed to generate 50 mN, 100 mN, and 180 mN after fixed. The bottom of Fig. 2(b) shows the motor assembly with the preload mechanism using a microspring. The sum of the stator, the rotor, and the preload mechanism weighs 37 mg.

Measuring the frequency response of the impedance shows the existence of the natural frequency: the impedance of the stator decreases when it resonates. This analysis is conducted by connecting the opposing piezoelectric plates to the high and low electrodes of the impedance analyzer (IM3570, Hioki E. E. Co., Japan). The impedance and phase are measured for the frequency ranging from 500 kHz to 700 kHz, where voltage amplitude is set constant at  $5 V_{p-p}$ . Fig. 3 shows an example of the measurements, where the resonant frequency for the bending mode is obtained at approximately 585 kHz.

## B. EXPERIMENTAL SETUP

Let us explain the experimental setup for the motor actuation. To drive the prototype motor, four contact probes supply power to the motor as shown in Fig. 4(a). The contact probes also support the four sides of the motor, and the motor is fixed to a jig. Fig. 4(c) shows the experimental setup for applying voltages to the motor. The two high-frequency voltages,  $E_1$  and  $E_2$ , are generated by using a 2-channel waveform

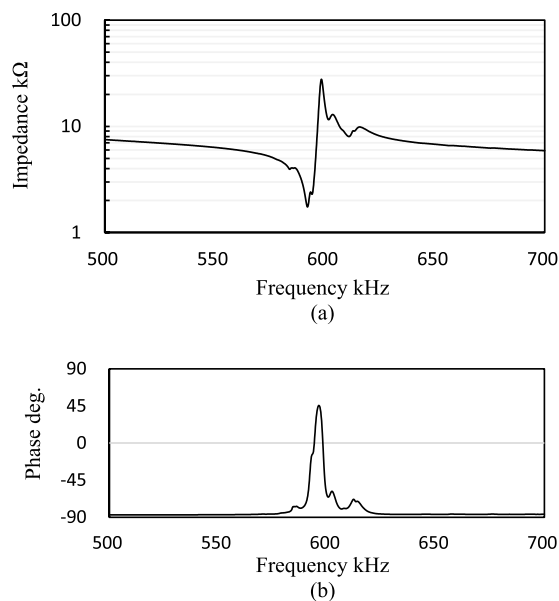


**FIGURE 3.** Frequency characteristics of (a) impedance and (b) phase of the stator.

generator (WF1974, NF Corp., Yokohama, Japan) and amplified by two high-frequency power amplifiers (BA4825, NF Corp.). In addition to the amplifiers, two transformers are also used to generate voltages with reversed phases by shifting the phase output by  $\pi$ . For example, when voltage  $E_1$  with a sine phase is input into the transformer, the negative sine phase voltage  $E_3$  is also output from the other terminal of the transformer. Thus, two voltages  $E_1$  and  $E_3$  are obtained from the same transformer. The same methodology also applies to cosine and negative cosine phase voltages  $E_2$  and  $E_4$ . Hence, by using two transformers, four types of voltages  $E_1$ – $E_4$  are applied to the piezoelectric plates PZT1–PZT4 adhered to the side surfaces of the stator, respectively. The amplitude and frequency of these voltages can be adjusted using the wave generator and amplifiers.

The rotational motion of the motor is recorded by a high speed camera (VW-9000, Keyence Co., Japan) with an image resolution of  $640 \times 320$  pixels at 4000 fps. A load with a diameter of 3 mm and a thickness of 1 mm ( $J = 7.2 \times 10^{-11} \text{ kgm}^2$ ) (Fig. 4(b)) is attached to the rotor end to reduce the angular acceleration of the motor. i.e., the lowered angular acceleration ensures that the measurement is accurate. A marker is attached to the load to track the rotational motion of the motor. By tracking the movement of the marker, a time-history data of the angular displacement can be accumulated, and angular velocity and acceleration can then be calculated through the time derivation of these data.

## C. EVALUATION OF THE MOTOR PERFORMANCE WITH PRELOADS

The transient response of the miniature ultrasonic motor is measured under the application of voltages with an amplitude of  $100 V_{p-p}$  and a frequency of 585 kHz, which is the natural

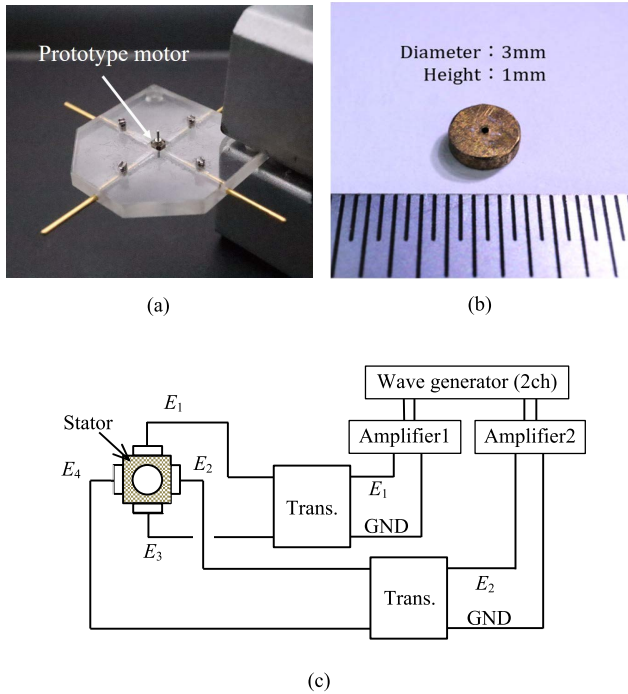


**FIGURE 4.** (a) Jig used to fix the motor. (b) A load attached to the rotor end. (c) Schematic of the experimental setup for applying voltages to the stator.

frequency of the first bending mode. Fig. 5(a), (b) and (c) show the transient responses for the motor with a preload  $N$  of 50 mN, 100 mN, and 180 mN, respectively. The plots obtained in the experiments are approximated to the first-order system expressed by the model in (1). The torque generated by the motor is calculated as the product of the angular acceleration and the moment of inertia of the load. In Fig. 5(a), a peak torque of approximately  $12 \mu\text{Nm}$  is obtained during the initial period of the rotation ( $t = 0-0.01$  s), and a peak angular velocity of over 2400 rad/s is shown during the steady-state ( $t = 0.05-0.10$  s). Fig. 5(b) shows a higher response than that with the smallest preload, indicating the increase in the torque. The improvement of the torque at higher preload enables a high-speed rotation of rotor blades in the next section. In Fig. 5(c), the torque is enhanced to approximately  $22 \mu\text{Nm}$  by a large preload of  $N = 180$  mN, but the angular velocity decreases to approximately 2200 rad/s. The motor efficiency, which is the ratio of the mechanical output to the electric input, increases to 2.9% at  $N = 180$  mN from 1.6% at  $N = 50$  mN. Fig. 5(d) summarizes the behavior of the angular velocity and the torque: the angular velocity decreases while the torque increases at a higher preload. This is because the motor torque depends on the Coulomb friction law, in which the friction force increases with the preload (i.e., normal force). The resultant torque increases in proportional to the preloads in the law, but a too high preload sharply reduces the motor output due to the high friction. Regarding the angular velocity, higher preloads suppress the vibration amplitude and results in a lower angular velocity. These characteristics are similar to

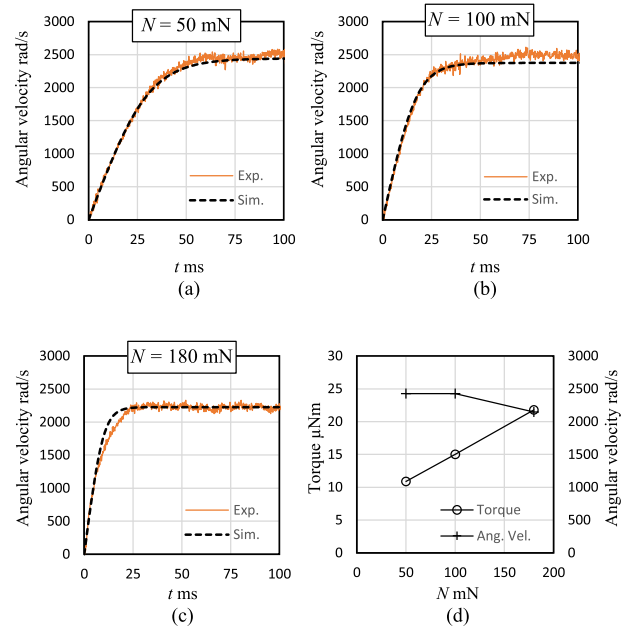


**FIGURE 5.** Transient response of the miniature ultrasonic motor for different preloads with a load attached. (a) Preload  $N = 50$  mN, (b)  $N = 100$  mN, (c)  $N = 180$  mN, and (d) the relation between the preload and the motor output.

the behaviors shown in the existing literature of macro-scale ultrasonic motors [32].

#### IV. FLIGHT TEST

##### A. MOTOR PERFORMANCE WITH ROTOR BLADES

On the basis of the performance measures obtained above, we select appropriate rotor blades to accomplish the flight demonstration. A short length of rotor blades requires a high-speed rotation for sufficient lift, and long rotor blades require a high torque to obtain a sufficient speed. Considering the case that the rotor blade model spins at  $\omega = 2000$  rad/s theoretically in (2), sufficient lift over the total weight can be obtained at a length of 20 mm ( $R = 10$  mm). From this estimation, rotor blades with a length of 20 mm (CX-STARS, Cheerson, China, see Fig. 6(a)) are selected for the prototype motor. Fig. 6(b) shows the assembly of the motor and the rotor blades. The rotor blades weigh approximately 60 mg, which are relatively heavy compared to the stator which only weighs 25 mg.

When the rotor blades spin, the anti-torque term increases in proportion to  $\omega^2$  in (5). In other words, high torque is required to obtain a sufficient angular velocity to fly. The angular velocity of the rotor blades is measured under the same experimental setup and conditions as in the previous section, where voltages with an amplitude of 100 V<sub>p-p</sub> and a frequency of 585 kHz are applied. Fig. 7(a), (b), and (c) show the transient responses for three different springs with a preload of  $N = 50$  mN, 100 mN and 180 mN, respectively. With an increase in the spring force, the motor generates higher torque and results in the higher angular velocity,

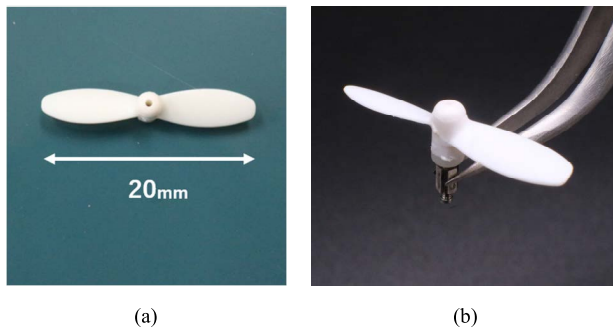


**FIGURE 6.** (a) Rotor blades with a wing span of 20 mm. (b) Assembly of the miniature ultrasonic motor and the rotor blade.

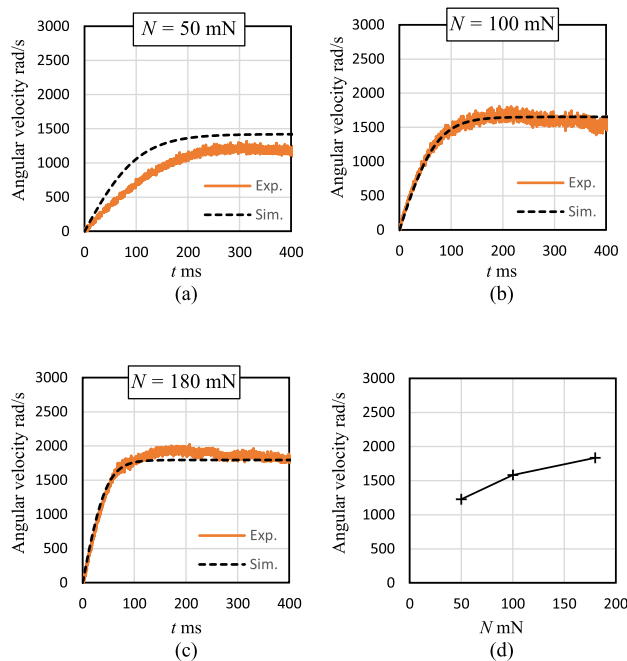


**FIGURE 7.** Transient response of the motor for different preloads with the rotor blade attached. (a) Preload  $N = 50$  mN, (b)  $N = 100$  mN, (c)  $N = 180$  mN, and (d) the relation between the preload and the angular velocity.

as shown in Fig. 7(d). The maximum preload of 180 mN results in a peak angular velocity of approximately 1830 rad/s at the steady-state. For numerical simulations, the inertia  $J_p$  and the torque coefficient  $C_Q$  in (5) are estimated as  $4.16 \times 10^{-10}$  kgm<sup>2</sup> and  $5.18 \times 10^{-3}$ , respectively. At a preload of 50 mN, a difference between the simulation and experiment curves is observed. This is likely because the weak preload makes the contact condition unstable. In the following sections, a motor with a preload of 180 mN is used for the experiments.

**B. LIFT GENERATION BY ROTOR BLADES**

Let us estimate the lift that the miniature flight device can generate. The thrust coefficient  $C_T$  in (2) can be obtained experimentally when a motor spins the rotor blades at a high speed. To know  $C_T$ , we have conducted an experiment in

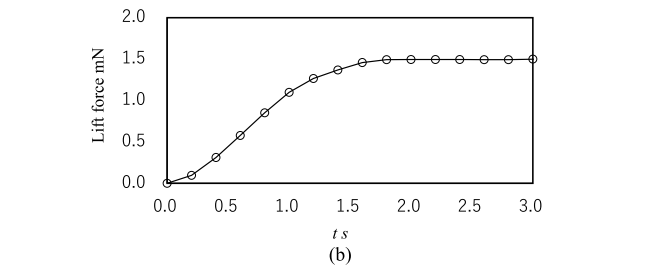
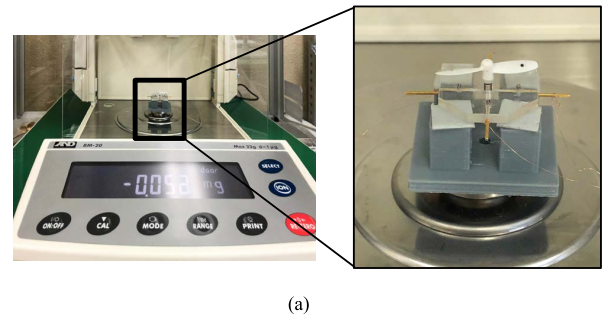


**FIGURE 8.** (a) Experimental setup for measuring the lift. (b) Lift measured using an electronic balance.

which an electromagnetic motor rotates the rotor blades. The resulting lift is approximately 19 mN (1.9 gf) at a rotational speed of 6280 rad/s, and  $C_T = 0.0125$  is obtained from (2). Considering the case of that the same rotor blades spin at a speed of approximately 1830 rad/s in (2), we can estimate a lift force of approximately 1.6 mN (0.16 gf). The chord  $c$  and radius  $R$  in (4) are determined from the dimensions of the blade as 3 mm and 10 mm, respectively. Using values  $C_Q$  and  $C_T$  mentioned above, section drag coefficient  $C_d = 0.18$  is obtained from (4). Since this value of  $C_d$  is appropriate even at a low Reynolds number [26], the estimated values of  $C_Q$  and  $C_T$  would be reasonable.

The lift generated by the rotor blades is too small to be accurately measured using force sensors, such as a strain gauge and a load cell. Hence, we use a precise electronic balance (BM-20, AND Discover Precision, Japan) to measure the lift. Although the electric balance needs a long time due to averaging and noise filtering, it is able to output the stable value of the lift with a resolution of 1  $\mu$ g. Fig. 8(a) shows the experimental setup for measuring the steady-state lift. The motor is fixed on a jig and placed on the electronic balance with the value being reset to zero. When voltages are applied, the value of the electronic balance decreases, and the reduced value is treated as the lift generated by the rotor blades spinning. Fig. 8(b) shows a time-history response of the lift force. These plots have been averaged at a time interval of 0.2 s by the electric balance. A peak lift of approximately 1.5 mN is obtained at the steady-state. The lift measured via the electronic balance is in rough agreement with the estimation in (2).

**C. POWER SUPPLY METHOD FOR THE STATOR**

To demonstrate the flight of the miniature flight device, a power supply must be considered. At the first, four wires

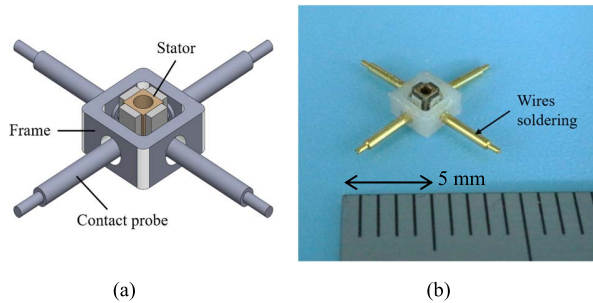


**FIGURE 9.** (a) Design of a small frame supported by four tiny contact probes. (b) The prototype frame assembled with the stator.

were soldered to the four piezoelectric plates, respectively. Soldering is the simplest process without additional components. The electric characteristics of the first bending vibration are evaluated by the frequency response of the impedance. The measurement is conducted by connecting the opposing piezoelectric plates (e.g., PZT1 and PZT3) to the high and low electrodes of the impedance analyzer (IM3570, Hioki E. E. Co., Japan), respectively. The resultant impedance characteristics showed that soldering process significantly damps the resonant vibration of the stator. At a resonant frequency of 585 kHz, the impedance of the motor increases from approximately 2.5 k $\Omega$  to 6.0 k $\Omega$ . The increase in the impedance blocks the current flowing through the motor, resulting in a significant dissipation in the motor performance. The most probable reason for this damping is that the existence of solder suppresses the vibration of the first bending mode.

A small frame shown in Fig. 9(a) is designed to avoid soldering directly to the piezoelectric plates. The frame has a width and a depth of 3.2 mm and a height of 1.5 mm. The four tiny contact probes with a diameter of 0.6 mm are attached to the frame by instant adhesive to serve as supports for fixing the motor. One end of contact probes has a concave tip, the edge of which contacts the electrode of the piezoelectric plates. Fig. 9(b) shows the prototype frame made of acetal plastic (POM), which is a material with high stiffness and good machinability. The entire frame weighs approximately 30 mg, which increases the total mass  $M$  of the device to approximately 110 mg. The lift obtained in previous subsection ( $T = 1.5$  mN ( $\approx 150$  mgf)) exceeds the total weight of the miniature flight device. For applying voltages, four wires with a diameter of 0.1 mm are then soldered to the four contact probes placed on the frame, respectively. These wires are wider than those of the other flying robots, such as [9]. This is because the wires support the position of the frame not to fall down, and prevent the reverse rotation caused by the anti-torque during the rotor blades spinning.

The frequency characteristics of the impedance of the motor installed to the frame shows the effectiveness. Fig. 10 compares it with the results of the soldering process, in which the wires are directly soldered to the piezoelectric

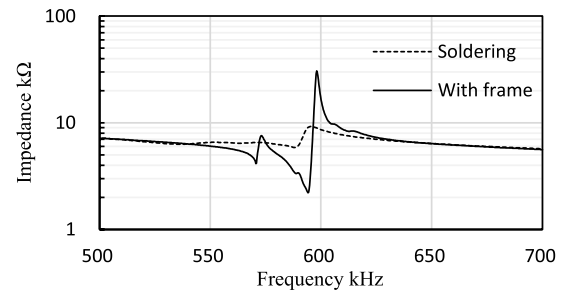


**FIGURE 10.** Frequency characteristics of the impedance: comparison between the stator after soldering and the stator placed into the designed frame.

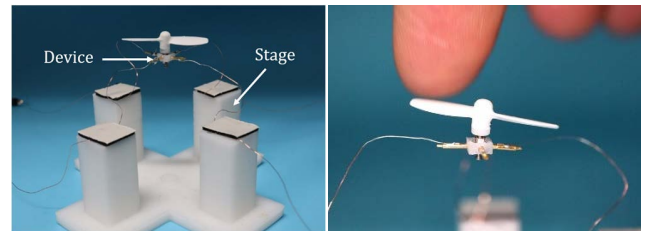


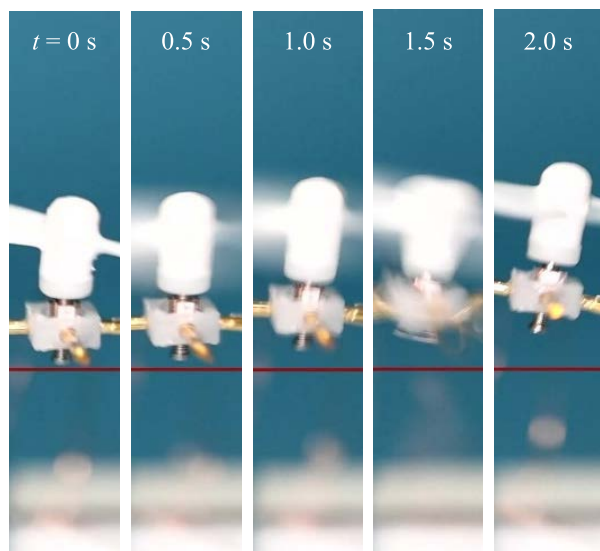
**FIGURE 11.** The miniature flight device and the experimental setup for the flight experiment.

elements. At the resonant frequency, the impedance of the motor remains constant at 2.5 k $\Omega$  in the case where the designed frame is used, despite of that the soldering damps the change in the impedance. Lower impedance supplies a larger current and results in a large vibration in the stator.

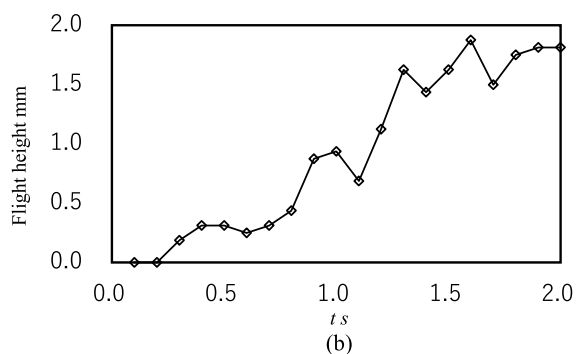
#### D. FLIGHT EXPERIMENT

Fig. 11 shows the experimental setup for flight experiment. A stage comprising four pillars supports the four wires of the motor. The wires are loosely fixed during the rotation. The device's motion is recorded using a camera under the application of voltages. Fig. 12(a) shows the state of the device at 0.5 s intervals during the flight experiment. A time-history of the flight height obtained via image processing is shown in Fig. 12(b). Although vibration caused by the anti-torque of the rotor blades is observed, a flight height of approximately 2 mm is achieved at  $t = 1.6$  s. Thus, the proposed miniature ultrasonic motor is indicated as feasible for use as an actuator when designing a rotary-wing PAV.

We note that, in the flight experiment, the forces acting on the device from the wires are quite large. The anti-torque  $Q$  is calculated as  $6.70 \times 10^{-6}$  Nm from (3) at an angular velocity of 1830 rad/s. Assuming that each wire is attached at a distance of 5 mm from the rotation axis, a force of at least 0.3 mN should be applied by each wire to keep the orientation of the device close to the initial one. The flight height of 2 mm in the experiment would be justified, because the elastic forces from the wires are also applied in the vertical direction, causing an external force  $F_e$  large enough to cancel the thrust in (6).



(a)



(b)

**FIGURE 12.** (a) State of the miniature flight device at 0.5 s intervals. (b) Flight height achieved by the device during the experiment.

## V. CONCLUSION

In this study, we investigated the feasibility of the 1–2 millimeter-scale ultrasonic motor for rotary-wing PAVs. The motor successfully rotated rotor blades with a length of 20 mm and could generate a lift that is capable of flying the entire device, although it was still tethered. The results presented herein are expected to be considerably helpful not only in the miniaturization of rotary-wing PAVs but to a wide range of miniature fluidic applications, such as micropumps and mixers using propellers.

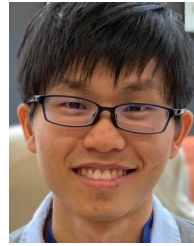
In the future, we will develop the design methodology to optimize the set of rotor blades and a miniature ultrasonic motor for a more powerful flight. The optimization requires more parameters, such as the stator shape and the dimensions of the piezoelectric materials, and the relationship between those dimensions and the motor power must be formulated. In addition to the optimal design, examining the contact between the stator and rotor is necessary to improve the efficiency and lifetime. The current stator contacts the rotor without coating although the commercial large-scale ultrasonic motors employ coatings to obtain

higher efficiency and a longer lifetime. When satisfied with the spec of PAVs, the miniature motor will be integrated into a silicon-based millimeter-scale circuit that makes the flying robot controllable.

## REFERENCES

- [1] D. Floreano and R. J. Wood, "Science, technology and the future of small autonomous drones," *Nature*, vol. 521, no. 7553, pp. 460–466, 2015, doi: [10.1038/nature14542](https://doi.org/10.1038/nature14542).
- [2] R. Wood, B. Finio, M. Karpelson, K. Ma, N. Pérez-Arancibia, P. Sreetharan, H. Tanaka, and J. Whitney, "Progress on 'pico' air vehicles," *Int. J. Robot. Res.*, vol. 31, no. 11, pp. 1292–1302, Sep. 2012, doi: [10.1177/0278364912455073](https://doi.org/10.1177/0278364912455073).
- [3] M. Hassanalian and A. Abdelkefi, "Classifications, applications, and design challenges of drones: A review," *Progr. Aerosp. Sci.*, vol. 91, pp. 99–131, May 2017, doi: [10.1016/j.paerosci.2017.04.003](https://doi.org/10.1016/j.paerosci.2017.04.003).
- [4] V. Kumar and N. Michael, "Opportunities and challenges with autonomous micro aerial vehicles," *Int. J. Robot. Res.*, vol. 31, no. 11, pp. 1279–1291, 2012, doi: [10.1177/0278364912455954](https://doi.org/10.1177/0278364912455954).
- [5] G. C. H. E. de Croon, M. A. Groen, C. De Wagter, B. Remes, R. Ruijsink, and B. W. van Oudheusden, "Design, aerodynamics and autonomy of the DelFly," *Bioinspiration Biomimetics*, vol. 7, no. 2, Jun. 2012, Art. no. 025003, doi: [10.1088/1748-3182/7/2/025003](https://doi.org/10.1088/1748-3182/7/2/025003).
- [6] M. Keennon, K. Klingebiel, and H. Won, "Development of the nano hummingbird: A tailless flapping wing micro air vehicle," in *Proc. 50th AIAA Aerosp. Sci. Meeting Including New Horizons Forum Aerosp. Expo.*, Jan. 2012, p. 588.
- [7] E. Farrell Helbling and R. J. Wood, "A review of propulsion, power, and control architectures for insect-scale flapping-wing vehicles," *Appl. Mech. Rev.*, vol. 70, no. 1, Jan. 2018, Art. no. 010801, doi: [10.1115/1.4038795](https://doi.org/10.1115/1.4038795).
- [8] M. H. Dickinson, F.-O. Lehmann, and S. P. Sane, "Wing rotation and the aerodynamic basis of insect flight," *Science*, vol. 284, no. 5422, pp. 1954–1960, 1999, doi: [10.1126/SCIENCE.284.5422.1954](https://doi.org/10.1126/SCIENCE.284.5422.1954).
- [9] R. J. Wood, "The first takeoff of a biologically inspired at-scale robotic insect," *IEEE Trans. Robot.*, vol. 24, no. 2, pp. 341–347, Apr. 2008, doi: [10.1109/TRO.2008.916997](https://doi.org/10.1109/TRO.2008.916997).
- [10] N. T. Jafferis, E. F. Helbling, M. Karpelson, and R. J. Wood, "Untethered flight of an insect-sized flapping-wing microscale aerial vehicle," *Nature*, vol. 570, no. 7762, pp. 491–495, Jun. 2019, doi: [10.1038/s41586-019-1322-0](https://doi.org/10.1038/s41586-019-1322-0).
- [11] D. Lentink and M. H. Dickinson, "Rotational accelerations stabilize leading edge vortices on revolving fly wings," *J. Experim. Biol.*, vol. 212, no. 16, pp. 2705–2719, Aug. 2009, doi: [10.1242/JEB.022269](https://doi.org/10.1242/JEB.022269).
- [12] M. Piccoli and M. Yim, "Piccolissimo: The smallest micro aerial vehicle," in *Proc. IEEE Int. Conf. Robot. Autom. (ICRA)*, May 2017, pp. 3328–3333, doi: [10.1109/ICRA.2017.7989378](https://doi.org/10.1109/ICRA.2017.7989378).
- [13] D. K.-C. Liu, J. Friend, and L. Yeo, "A brief review of actuation at the micro-scale using electrostatics, electromagnetics and piezoelectric ultrasonics," *Acoust. Sci. Technol.*, vol. 31, no. 2, pp. 115–123, 2010, doi: [10.1250/AST.31.115](https://doi.org/10.1250/AST.31.115).
- [14] T. Mashimo and S. Izuhara, "Review: Recent advances in micromotors," *IEEE Access*, vol. 8, pp. 213489–213501, 2020, doi: [10.1109/ACCESS.2020.3041457](https://doi.org/10.1109/ACCESS.2020.3041457).
- [15] A. Inoue, B. Shen, and A. Takeuchi, "Developments and applications of bulk glassy alloys in late transition metal base system," *Mater. Trans.*, vol. 47, no. 5, pp. 1275–1285, 2006, doi: [10.2320/MATER-TRANS.47.1275](https://doi.org/10.2320/MATER-TRANS.47.1275).
- [16] W. S. N. Trimmer, "Microrobots and micromechanical systems," *Sens. Actuators*, vol. 19, no. 3, pp. 267–287, 1989, doi: [10.1016/0250-6874\(89\)87079-9](https://doi.org/10.1016/0250-6874(89)87079-9).
- [17] E. Drexler, *Nanosystems: Molecular Machinery, Manufacturing, and Computation*. Hoboken, NJ, USA: Wiley, 1992.
- [18] K. Dermitzakis, J. P. Carbajal, and J. H. Marden, "Scaling laws in robotics," *Proc. Comput. Sci.*, vol. 7, pp. 250–252, Jan. 2011, doi: [10.1016/j.procs.2011.09.038](https://doi.org/10.1016/j.procs.2011.09.038).
- [19] L.-S. Fan, Y.-C. Tai, and R. S. Müller, "IC-processed electrostatic micromotors," *Sens. Actuators*, vol. 20, nos. 1–2, pp. 41–47, 1989, doi: [10.1016/0250-6874\(89\)87100-8](https://doi.org/10.1016/0250-6874(89)87100-8).
- [20] S. C. Jacobsen, R. H. Price, J. E. Wood, T. H. Rytting, and M. Rafaelof, "The wobble motor: Design, fabrication and testing of an eccentric-motion electrostatic microactuator," in *Proc. Int. Conf. Robot. Autom.*, May 1989, pp. 1536–1546, doi: [10.1109/ROBOT.1989.100197](https://doi.org/10.1109/ROBOT.1989.100197).

- [21] T. Morita, "Miniature piezoelectric motors," *Sens. Actuators A, Phys.*, vol. 103, no. 3, pp. 291–300, Feb. 2003, doi: [10.1016/S0924-4247\(02\)00405-3](https://doi.org/10.1016/S0924-4247(02)00405-3).
- [22] B. Watson, J. Friend, and L. Yeo, "Piezoelectric ultrasonic micro/millimeter-scale actuators," *Sens. Actuators A, Phys.*, vol. 152, no. 2, pp. 219–233, Jun. 2009, doi: [10.1016/j.sna.2009.04.001](https://doi.org/10.1016/j.sna.2009.04.001).
- [23] *Website of New Scale Technologies*. Accessed: Sep. 9, 2021. [Online]. Available: <https://www.newscaletech.com/resources/technology/squiggle-micro-motor-technology/>
- [24] T. Mashimo, "Miniature preload mechanisms for a micro ultrasonic motor," *Sens. Actuators A, Phys.*, vol. 257, pp. 106–112, Apr. 2017, doi: [10.1016/j.sna.2017.02.009](https://doi.org/10.1016/j.sna.2017.02.009).
- [25] E. T. K. Chiang and T. Mashimo, "Comparison study of bending and three-wave vibration modes for micro ultrasonic motors," *Sens. Actuators A, Phys.*, vol. 329, Oct. 2021, Art. no. 112801, doi: [10.1016/j.sna.2021.112801](https://doi.org/10.1016/j.sna.2021.112801).
- [26] R. Y. Hutama, M. M. Khalil, and T. Mashimo, "A millimeter-scale rolling microrobot driven by a micro-gear ultrasonic motor," *IEEE Robot. Autom. Lett.*, vol. 6, no. 4, pp. 8158–8164, Oct. 2021, doi: [10.1109/LRA.2021.3104227](https://doi.org/10.1109/LRA.2021.3104227).
- [27] T. Morita, H. Toshiro, and M. K. Kurosawa, "A cylindrical shaped micro ultrasonic motor utilizing PZT thin film (1.4 mm in diameter and 5.0 mm long stator transducer)," *Sens. Actuators A, Phys.*, vol. 83, nos. 1–3, pp. 225–230, May 2000, doi: [10.1016/S0924-4247\(99\)00388-X](https://doi.org/10.1016/S0924-4247(99)00388-X).
- [28] T. Kanda, A. Makino, T. Ono, K. Suzumori, T. Morita, and M. K. Kurosawa, "A micro ultrasonic motor using a micro-machined cylindrical bulk PZT transducer," *Sens. Actuators A, Phys.*, vol. 127, no. 1, pp. 131–138, Feb. 2006, doi: [10.1016/j.sna.2005.10.056](https://doi.org/10.1016/j.sna.2005.10.056).
- [29] T. Mashimo and K. Terashima, "Dynamic analysis of an ultrasonic motor using point contact model," *Sens. Actuators A, Phys.*, vol. 233, pp. 15–21, Sep. 2015, doi: [10.1016/j.sna.2015.05.009](https://doi.org/10.1016/j.sna.2015.05.009).
- [30] M. Okamoto, K. Yasuda, and A. Azuma, "Aerodynamic characteristics of the wings and body of a dragonfly," *J. Experim. Biol.*, vol. 199, no. 2, pp. 281–294, Feb. 1996, doi: [10.1242/jeb.199.2.281](https://doi.org/10.1242/jeb.199.2.281).
- [31] J. G. Leishman, *Principles of Helicopter Aerodynamics*. Cambridge, U.K.: Cambridge Univ. Press, 2006.
- [32] T. Mashimo and K. Terashima, "Experimental verification of elliptical motion model in traveling wave ultrasonic motors," *IEEE/ASME Trans. Mechatron.*, vol. 20, no. 6, pp. 2699–2707, Dec. 2015, doi: [10.1109/TMECH.2015.2392126](https://doi.org/10.1109/TMECH.2015.2392126).



**ERIC TAN KAI CHIANG** (Member, IEEE) received the B.E. and M.E. degrees from the Toyohashi University of Technology, Japan, in 2019 and 2021, respectively. He is currently a Mechanical Engineer at KIOXIA Corporation. His research interest includes micro piezoelectric actuators.



**TAKATERU URAKUBO** (Member, IEEE) received the B.E., M.E., and Ph.D. degrees in aeronautics and astronautics from Kyoto University, Kyoto, Japan, in 1996, 1998, and 2001, respectively. In 2001, he joined Kobe University, Kobe, Japan, as an Assistant Professor, where he is currently an Associate Professor with the Graduate School of System Informatics. From 2007 to 2009, he was a Visiting Research Scientist at Carnegie Mellon University, Pittsburgh, PA, USA. His current research interests include non-linear dynamical systems, non-linear control theory, and autonomous robots.



**TOMOAKI MASHIMO** (Member, IEEE) received the Ph.D. degree in mechanical engineering from the Tokyo University of Agriculture and Technology, Japan, in 2008. He was a Robotics Researcher at The Robotics Institute, Carnegie Mellon University, Pittsburgh, PA, USA, from 2008 to 2010. In 2011, after being an Assistant Professor (Tenure-Track) at the Toyohashi University of Technology, he became an Associate Professor, in 2016. His research interests include piezoelectric actuators and robotic applications.

• • •